ROYAL SOCIETY OF CHEMISTRY

PAPER

Check for updates

Activating rhodium phosphide-based catalysts for the pH-universal hydrogen evolution reaction†

Zonghua Pu,[a] Ibrahim Saana Amiinu,[a] Daping He,[a,b] Min Wang,[a] Guoqiang Li (ID) *[c] and Shichun Mu (ID) *[a]

Highly active and stable Pt-free electrocatalysts for hydrogen production *via* water splitting are of great demand for future energy systems. Herein, we report a novel hydrogen evolution reaction (HER) catalyst consisting of rhodium phosphide (Rh_2P) nanoparticles as the core and N-doped carbon (NC) as the shell ($Rh_2P@NC$). In a wide pH range, our catalyst not only possesses a small overpotential at 10 mA cm^{-2} (~9 mV in 0.5 M H_2SO_4, ~46 mV in 1.0 M PBS and ~10 mV in 1.0 M KOH), but also demonstrates high stability. Importantly, all these performances are far superior to commercial Pt/C catalysts for HER. To the best of our knowledge, this is the highest HER performance reported so far in acidic and basic media. Density functional theory (DFT) calculations reveal that the introduction of phosphorus can significantly lower the proton adsorption energy of Rh/NC, thereby benefiting surface hydrogen generation. Moreover, this synthetic strategy for $Rh_2P@NC$ is also applied to other transition metal phosphides (TMPs)/nitrogen-doped carbon heterostructures (such as $Ru_2P@NC$, $Fe_2P@NC$, WP@NC *etc.*) with advanced performance toward HER and beyond.

Hydrogen is a promising alternative energy carrier to fossil fuels due to its renewability, zero-emission and high gravimetric energy density.[1,2] Although the electrolysis of water is an eco-friendly and sustainable pathway to hydrogen generation,[3,4] it needs an effective electrocatalyst for both the hydrogen evolution reaction (HER) and oxygen evolution reaction (OER). Currently, platinum (Pt) is still the most active electrocatalyst for HER.[5] However, the high-price and scarcity of Pt limit its wide application in electrolyzers.[6,7] In recent years, considerable efforts have been made to develop highly-active, stable, and cost-effective HER catalysts.[8–14] Nevertheless, their catalytic activity is still far from satisfactory in comparison with Pt, which would increase energy consumption and hence decrease economic competitiveness.[15,16] As a result, developing a Pt-free catalyst with similar or superior activity to Pt is highly desirable.

The past few years have witnessed the rapid development of transition metal phosphides (TMPs, M = Cu, Mo, Fe, W,

Co and Ni) for efficient HER catalysis in acidic solutions.[17–21] Despite such a big success, it still remains a huge challenge to design and develop TMPs catalysts with superior activity to Pt and long-term electrochemical durability at all pH values, which is critical for practical applications. Myoinositol 1,2,3,4,5,6-hexakisphosphate (MH) (Fig. S1†) is a nontoxic, natural, eco-friendly and renewable biological compound. It contains six phosphate groups that can act as a P source and also readily cross-link the metal precursors.[22–24] In addition, previous studies have demonstrated that the catalyst coated with a carbon shell, especially heteroatom-doped carbon (N and/or P), can simultaneously promote the HER activity through synergism and enhance the durability due to the protection from the carbon cage.[25–29]

Herein, for the first time, we successfully achieved Rh_2P nanoparticle encapsulated N-doped carbon (NC) ($Rh_2P@NC$) core-shell frameworks *via* a one-step facile solid-state reaction with $RhCl_3 \cdot xH_2O$, MH and melamine as Rh, P and C sources (Scheme 1). Electrochemical measurements show that $Rh_2P@NC$ has an unprecedented high electrocatalytic performance toward HER under acidic, neutral, and basic conditions, even superior to that of commercial Pt/C catalysts.

Fig. 1a presents the low-magnification transmission electron microscopy (TEM) image of $Rh_2P@NC$, indicating that a large amount of Rh_2P nanoparticles are decorated on thin carbon nanosheets. In addition, Rh_2P nanoparticles have a small size generally less than 60 nm (Fig. S2†). The high-magnification TEM image (Fig. 1b) shows the encapsulated

[a]State Key Laboratory of Advanced Technology for Materials Synthesis and Processing, Wuhan University of Technology, Wuhan 430070, P. R. China. E-mail: msc@whut.edu.cn
[b]Hubei Engineering Research Center of RF-Microwave Technology and Application, Wuhan University of Technology, Wuhan 430070, P. R. China
[c]Department of Electronic Materials, South China University of Technology, Guangzhou 510641, P. R. China. E-mail: msgli@scut.edu.cn
†Electronic supplementary information (ESI) available. See DOI: 10.1039/c8nr02854k
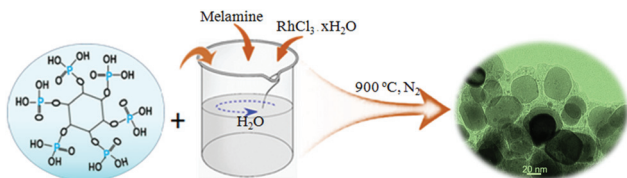
Scheme 1 Schematic illustration of the synthesis process of the Rh₂P@NC electrocatalyst.

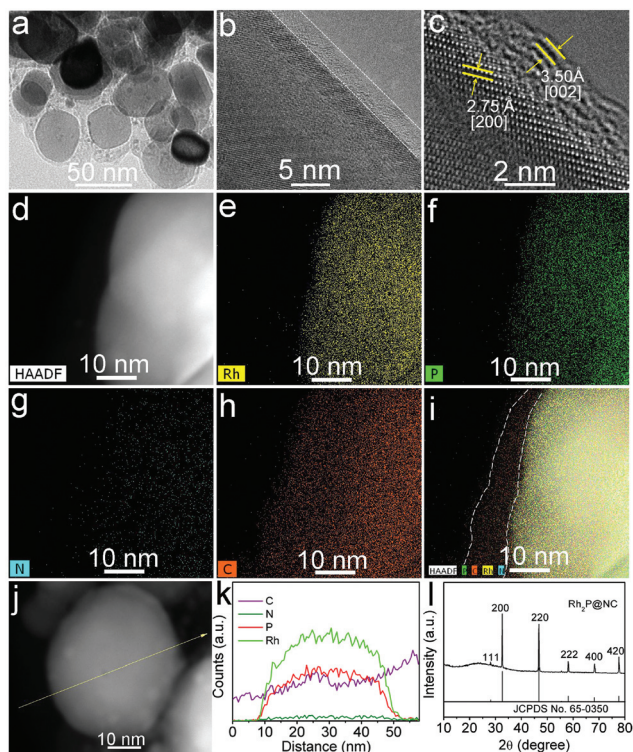**Fig. 1** (a and b) TEM and (c) HRTEM images of Rh₂P@NC. (d–i) HAADF images and EDX elemental mapping of Rh, P, N and C for Rh₂P@NC. (j) HAADF-STEM image of Rh₂P@NC with the yellow line showing the line scanning path. (k) Corresponding line-scanning profile. (l) XRD pattern of Rh₂P@NC.

relationship between Rh₂P and the carbon matrices in the formed core–shell structure. The high resolution TEM (HRTEM) (Fig. 1c) image reveals clear fringes with a lattice spacing of 2.75 Å, which can be indexed to the (200) plane of cubic Rh₂P. Furthermore, the observed 3.50 Å lattice fringe is in good agreement with the (002) plane of graphite. High-angle annular dark-field scanning transmission electron microscopy-energy-dispersive X-ray spectroscopy (HAADF-STEM-EDX) line scan and elemental mapping analysis confirm the homogeneous distribution of Rh, P, N, and C elements (Fig. 1d–k). Most importantly, the core (Rh₂P) and shell (NC) composition can be clearly seen (Fig. 1i). The crystal structure of the obtained sample was characterized by X-ray powder diffraction (XRD). The diffraction peaks at $2\theta = 28.1$, 32.5, 46.6, 58.0, 68.1 and 77.5° can be well-indexed to the

(111), (200), (220), (222), (400) and (420) planes of cubic Rh₂P (JCPDS No. 65-0350, space group: $Fm\bar{3}m$, $a_o = b_o = c_o = 5.502$ Å) (Fig. 1l). The N-doped carbon layers were further characterized by Raman and X-ray photoelectron spectroscopy (XPS). As shown in Fig. S3a,† Rh₂P@NC displays two Raman peaks at ~1353 and 1590 cm⁻¹, which correspond to the D and G bands, respectively. In the high-resolution XPS spectrum (Fig. S3b†), the C 1s peaks at 288.9, 285.8 and 284.5 eV can be assigned to carbon in the form of O=C–O, C=O and C–C, respectively.[30] The high resolution N 1s spectrum (Fig. S3c†) can be deconvoluted into three individual subpeaks, corresponding to oxidized-N (402.3 eV), pyrrolic-N (400.2 eV) and pyridinic-N (398.5 eV).[31] As a result, we successfully synthesised the Rh₂P@NC core–shell structure catalyst. For comparison, the same preparation method without the presence of MH only leads to the formation of Rh/NC (Fig. S4†).

Next, we evaluated the HER catalytic performance of Rh₂P@NC in 0.5 M of H₂SO₄ solution using a typical three electrode system. The Rh/NC and commercial Pt/C (20 wt%) were also tested under the same conditions for comparison. The loading amount of Rh in Rh₂P@NC for catalytic measurements is about 0.07 mg cm⁻² determined by inductively coupled plasma atomic emission spectrometry (ICP-AES), which is lower than Pt in Pt/C (~0.14 mg cm⁻²). Before the tests, the reference electrode was calibrated in a high purity hydrogen saturated electrolyte solution with a Pt wire as the working electrode (Fig. S5†). Fig. 2a shows the representative HER polarization curves. Both Rh₂P@NC and Pt/C exhibit outstanding HER catalytic activities with 0 mV onset overpotential (η_{onset}), which is much smaller than that of Rh/NC. Rh₂P@NC
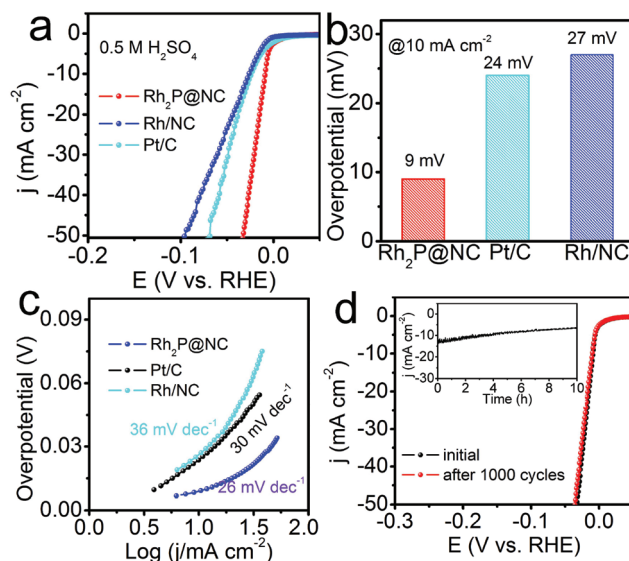

Fig. 2 Electrocatalytic properties of HER in 0.5 M H₂SO₄. (a) Polarization curves of Rh₂P@NC, Rh/NC and Pt/C, recorded at 5 mV s⁻¹. (b) Corresponding overpotentials at 10.0 mA cm⁻² current density. (c) Corresponding Tafel slopes. (d) Polarization curves for Rh₂P@NC initially and after 1000 CV scanning between +0.26 and −0.14 V vs. RHE. (Inset: Time-dependent current density curve for Rh₂P@NC under a static overpotential of 20 mV for 10 h, without iR correction.)

only needs an overpotential (η_{10}) as low as 9 mV (16 mV without iR correction, Fig. S6†) at a current density of 10 mA cm^{-2}, which is about 15 and 18 mV lower than Pt/C and Rh/NC (Fig. 2b), respectively. It should be noted that when Rh$_2$P@NC is loaded on carbon cloth, an overpotential of 8 mV is needed at j = 10 mA cm^{-2} (Fig. S7†). The corresponding Tafel slope of Rh$_2$P@NC is ~26 mV dec^{-1}, appreciably lower than that of commercial Pt/C (30 mV dec^{-1}) (Fig. 2c), suggesting the improved HER kinetics of Rh$_2$P@NC which is executed via the Volmer–Tafel mechanism.[32] Both the overpotential of Rh$_2$P@NC at 10 mA cm^{-2} and the Tafel slope are lower than that of commercial Pt/C and all of the noble metals, non-noble metals and nonmetallic catalysts reported under acidic conditions (Table S1†). Based on the Tafel analysis, the calculated exchange current density (j_0) of Rh$_2$P@NC is approximately 2.5×10^{-3} A cm^{-2} (Fig. S8†), which is higher than that of Pt/C (1.5×10^{-3} A cm^{-2}),[32] further revealing the exceptional H$_2$ evolution efficiency of Rh$_2$P@NC.

Besides the high catalytic activity, optimal stability is also needed for the application of catalysts. Therefore, the stability was evaluated under acidic media. As shown in Fig. 2d, after 1000 cyclic voltammetric (CV) cycles between +0.26 and −0.14 V vs. RHE at a scan rate of 100 mV s^{-1} in 0.5 M H$_2$SO$_4$ solution, the polarization curve retains almost similar performance to the initial test. For comparison, Pt/C was also tested under the same conditions. The polarization curve of Pt/C shifts negatively by about ~11 mV after 1000 CV cycles at a current density of 10 mA cm^{-2}, suggesting a significant decrease in the catalytic activity (Fig. S9†). Furthermore, the long-term stability of Rh$_2$P@NC was assessed by electrolysis at a fixed overpotential of 20 mV without iR correction. Rh$_2$P@NC displays a slight hydrogen evolution current density loss after 10 h (inset of Fig. 2d). The Rh$_2$P@NC catalyst after the HER stability test was collected and characterized by TEM. The TEM image (Fig. S10†) confirms that the size and morphology of the Rh$_2$P NPs are maintained well. All of these suggest that the N-doped carbon shell contributes to protecting the catalysts from corrosion during cycling and enhances the conductivity.[16,27] These results confirm that Rh$_2$P@NC is stable for long-term hydrogen generation by the electrolysis of water, making it a promising catalyst for widespread commercialization.

We further tested the activity of Rh$_2$P@NC in neutral and alkaline electrolytes. In 1.0 M phosphate buffered saline (PBS) (pH = 7), Rh$_2$P@NC exhibits excellent catalytic behavior with an onset overpotential of 0 mV, a Tafel slope of 37 mV dec^{-1}, and good stability (Fig. 3a–c). To reach the current density of 10 mA cm^{-2}, Rh$_2$P@NC only needs an overpotential of 46 mV (inset of Fig. 3a). More interestingly, such catalytic behavior is better than that of Pt/C (η_{10} = 56 mV, Tafel slope: 42 mV dec^{-1}) and Rh/NC (η_{10} = 154 mV, Tafel slope: 97 mV dec^{-1}) as well as all of the Pt-free HER catalysts reported in neutral solutions (Table S1†). In addition, as shown in Fig. 3d, the Rh$_2$P@NC catalyst also exhibits high HER catalytic activity than that of Pt/C in 1.0 M KOH, affording a current density of 10 mA cm^{-2} at an overpotential of 10 mV, which is 4 and 14 mV lower than that of Pt/C and Rh/NC (inset of Fig. 3d), respectively. Such an
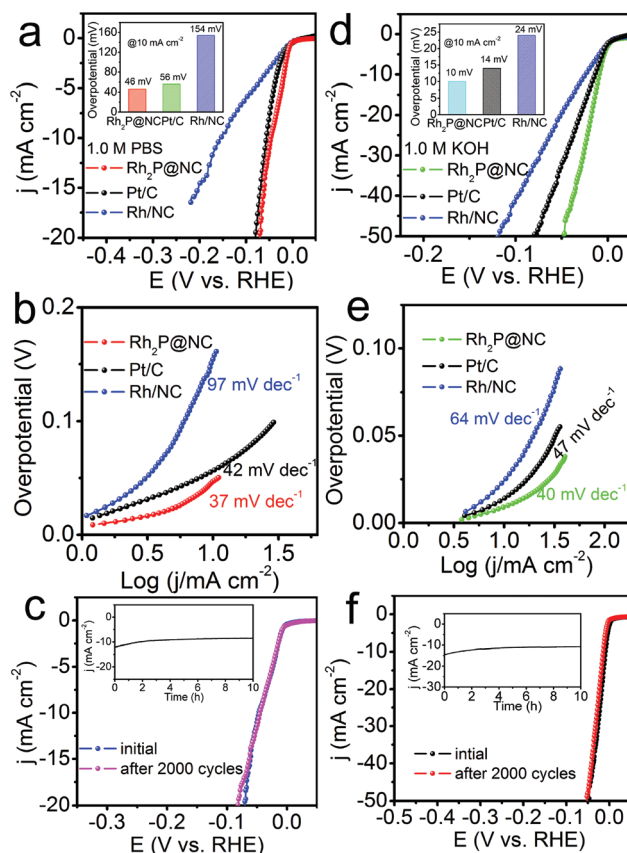

Fig. 3 Electrocatalytic properties of HER in 1.0 M PBS and KOH. (a, d) Polarization curves for Rh$_2$P@NC, Rh/NC and Pt/C, recorded at 5 mV s^{-1} (inset of a and b: corresponding overpotentials at 10.0 mA cm^{-2} current density.). (b, e) Corresponding Tafel slopes. (c, f) Polarization curves for Rh$_2$P@NC initially and after 1000 CV scanning between +0.26 and −0.14 V vs. RHE. (Inset: Time-dependent current density curve for Rh$_2$P@NC under static overpotentials of 60 and 20 mV for 10 h in neutral and alkaline solutions, respectively. Without iR correction.)

impressive overpotential and a low Tafel slope of 40 mV dec^{-1} (Fig. 3e) indicate that Rh$_2$P@NC is also a promising electrocatalyst for HER even in alkaline media in comparison with all of the recently developed noble metals, non-noble metals and nonmetallic HER electrocatalysts (Table S1†). Similarly, Rh$_2$P@NC displays an excellent stability in basic solution (Fig. 3f). Furthermore, the hydrogen yield catalyzed by Rh$_2$P@NC was measured. As shown in Fig. 4, it indicates almost 100% faradaic efficiency for hydrogen production over the whole pH range.[33] Overall, these results clearly indicate the superior catalytic performance and durability of Rh$_2$P@NC toward HER at all pH values.

The superior HER activity and stability of Rh$_2$P@NC in a wide pH range could be attributed to the following attributes: first, phosphorus plays a crucial role in determining the robust catalytic properties. On one hand, as shown in Fig. 5a, Rh/NC yields a calculated ΔG_{H^*} of −0.24 eV, indicating strong hydrogen binding strength on the catalyst surface and a sluggish hydrogen releasing step. However, after introducing phos-
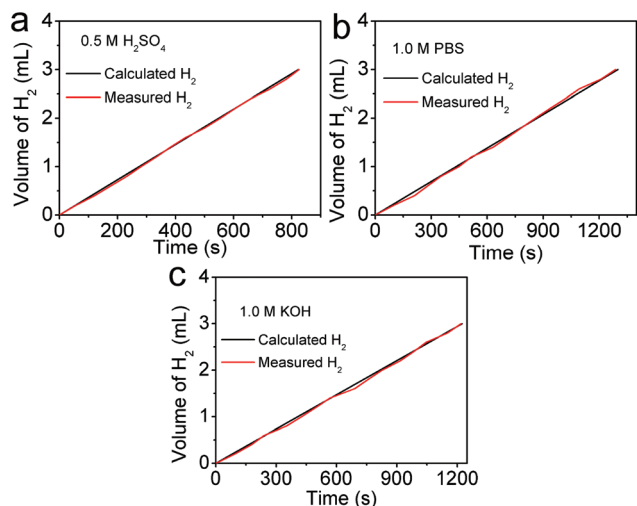
Fig. 4 Hydrogen production efficiencies under potentiostatic electrolysis with Rh₂P@NC under (a) 0.5 M H₂SO₄, (b) 1.0 MPBS, and (c) 1.0 M KOH solutions. The calculated H₂ lines represent the theoretical amount of H₂ assuming a quantitative faradaic yield (black line). The measured H₂ lines represent the experimentally measured amount of H₂ (red line).
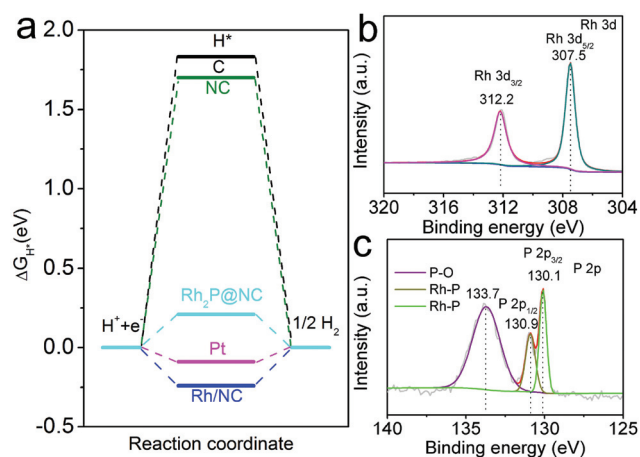

Fig. 5 (a) Calculated free energy diagram of the catalyst samples. (b) Rh 3d and (c) P 2p XPS spectra of Rh₂P@NC.

130.1 eV corresponding to the binging energy (BE) of P $2p_{1/2}$ and P $2p_{3/2}$ as well as a peak at 133.7 eV for P–O.[37] The BE of 307.5 eV for Rh $3d_{5/2}$ exhibits a positive shift from that of metallic Rh (307.3 eV),[38] while the BE of 130.1 eV for P $2p_{3/2}$ exhibits a negative shift from that of elemental P (130.2 eV).[39] These observations suggest that Rh in Rh₂P@NC bears a partial positive charge (δ^+) and P in Rh₂P@NC bears a partial negative charge (δ^-). These findings point to a weak electron transfer from Rh to P in Rh₂P@NC. Second, the uniform encapsulation of the Rh₂P nanoparticles within the conductive NC layers enables full utilization of the active sites of the catalysts and protection against solution induced corrosion.[40,41] Third, the synergistic effect between Rh₂P and NC might further enhance the HER catalytic activity.[42] Eventually, the unique nanostructure of the NC encapsulating the Rh₂P nanoparticles not only avoids the aggregation of Rh₂P nanoparticles, but also guarantees the high durability of the electrocatalyst during a long-term operation.[43,44]

Additionally, the developed strategy was also effective in preparing a series of transition metal phosphides/nitrogen-doped carbon materials (*e.g.* Ru₂P@NC, Fe₂P@NC and WP@NC). The typical XRD patterns and TEM images of the as-prepared Ru₂P@NC, WP@NC and Fe₂P@NC are shown in Fig. 6. These demonstrate the generality of the synthetic strategy.
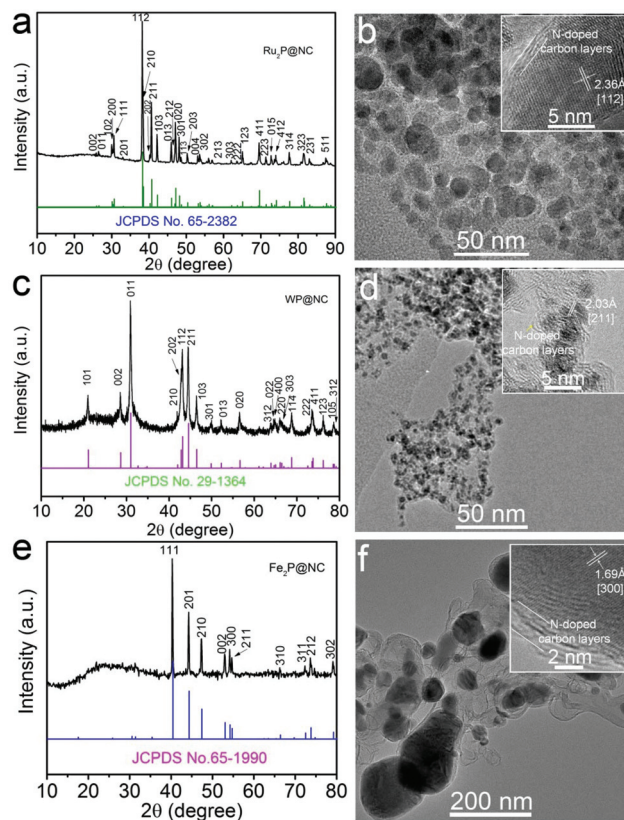
phorus, the formed Rh₂P@NC dramatically lowers the proton adsorption energy ($\Delta G_{H^*} = 0.20$ eV), thereby benefitting the H₂ generation process. On the other hand, according to previous analysis, the researchers found that there is significant covalent interaction between P and Rh.[34] As a result, the H-binding strength is neither too strong nor too weak, making Rh₂P possess an ultrahigh electrocatalytic performance toward HER.[34,35] In addition, herein, XPS was employed to investigate the interaction between P and Rh in Rh₂P@NC. Fig. 5b and c illustrate the XPS spectra of the Rh and P regions in Rh₂P@NC, respectively. The two peaks at 312.2 and 307.5 eV are assigned to Rh $3d_{3/2}$ and Rh $3d_{5/2}$, respectively.[36] The high-resolution spectrum of P 2p shows two subpeaks at 130.9 and

Fig. 6 (a) XRD pattern and (b) TEM images of Ru₂P@NC. (c) XRD pattern and (d) TEM images of WP@NC. (e) XRD pattern and (f) TEM images of Fe₂P@NC.

Conclusions

In summary, we have developed a facile strategy to synthesize Rh_2P nanoparticles encapsulated in a N-doped carbon (NC) ($Rh_2P@NC$) core–shell structure. Electrochemical measurements demonstrate that $Rh_2P@NC$ was a robust and durable HER electrocatalyst in acidic, neutral and alkaline media. $Rh_2P@NC$ possessed a low overpotential at 10 mA cm^{-2} (~9 mV in 0.5 M H_2SO_4, ~46 mV in 1.0 M PBS and ~10 mV in 1.0 M KOH). Such a high HER activity is much better than that of commercial Pt/C. In addition, $Rh_2P@NC$ exhibited better long-term stability than Pt/C under similar conditions. This is the first study on a transition metal phosphide/heteroatom-doped carbon hybrid material with HER catalytic activity exceeding that of the Pt catalyst over a wide pH range. This effective method might be extended to the design and preparation of other transition metal phosphide/heteroatom-doped carbon materials (e.g. $Ru_2P@NC$, $Fe_2P@NC$ and $WP@NC$) for various electrocatalytic applications.

Conflicts of interest

There are no conflicts to declare.

Acknowledgements

Notes and references

1 M. Balat and H. Balat, *Energy Sources, Part A*, 2009, **31**, 1280–1293.
2 G. W. Crabtree, M. S. Dresselhaus and M. V. Buchanan, *Phys. Today*, 2004, **57**, 39–44.
3 J. A. Turner, *Science*, 2004, **305**, 972–974.
4 M. S. Dresselhaus and I. L. Thomas, *Nature*, 2001, **414**, 332–337.
5 V. R. Stamenkovic, B. S. Mun, M. Arenz, K. J. J. Mayrhofer, C. A. Lucas, G. Wang, P. N. Ross and N. M. Markovic, *Nat. Mater.*, 2007, **6**, 241–247.
6 M. G. Walter, E. L. Warren, J. R. McKone, S. W. Boettcher, Q. X. Mi, E. A. Santori and N. S. Lewis, *Chem. Rev.*, 2010, **110**, 6446–6473.
7 J. R. McKone, E. L. Warren, M. J. Bierman, S. W. Boettcher, B. S. Brunschwig, N. S. Lewis and H. B. Gray, *Energy Environ. Sci.*, 2011, **4**, 3573–3583.
8 C. G. Morales-Guio, L. A. Stern and X. Hu, *Chem. Soc. Rev.*, 2014, **43**, 6555–6569.
9 E. J. Popczun, J. R. McKone, C. G. Read, A. J. Biacchi, A. M. Wiltrout, N. S. Lewis and R. E. Schaak, *J. Am. Chem. Soc.*, 2013, **135**, 9267–9270.
10 Q. Liu, J. Tian, W. Cui, N. Cheng, A. M. Asiri and X. Sun, *Angew. Chem., Int. Ed.*, 2014, **53**, 6710–6714.
11 Y. Xu, M. Gao, Y. Zheng, J. Jiang and S. Yu, *Angew. Chem., Int. Ed.*, 2013, **52**, 8546–8550.
12 Z. Pu, Y. Xue, I. S. Amiinu, Z. Tu, X. Liu, W. Li and S. Mu, *J. Mater. Chem. A*, 2016, **4**, 15327–15332.
13 D. Kong, H. Wang, Z. Lu and Y. Cui, *J. Am. Chem. Soc.*, 2014, **136**, 4897–4900.
14 B. You and Y. Sun, *ChemPlusChem*, 2016, **81**, 1045–1055.
15 M. M. Rashid, M. K. Mesfer Al, H. Naseem and M. Danish, *Int. J. Eng. Adv. Technol.*, 2015, **4**, 2249–8958.
16 J. Su, Y. Yang, G. Xia, J. Chen, P. Jiang and Q. Chen, *Nat. Commun.*, 2017, **8**, 14969.
17 Y. Shi and B. Zhang, *Chem. Soc. Rev.*, 2016, **45**, 1529–1541.
18 J. F. Callejas, C. G. Read, C. W. Roske, N. S. Lewis and R. E. Schaak, *Chem. Mater.*, 2016, **28**, 6017–6044.
19 C. Tang, R. Zhang, W. Lu, L. He, X. Jiang, A. M. Asiri and X. Sun, *Adv. Mater.*, 2017, **29**, 1602441.
20 J. M. McEnaney, J. C. Crompton, J. F. Callejas, E. J. Popczun, A. J. Biacchi, N. S. Lewis and R. E. Schaak, *Chem. Mater.*, 2014, **26**, 4826–4831.
21 M. Sun, H. Liu, J. Qu and J. Li, *Adv. Energy Mater.*, 2016, **6**, 1600087.
22 L. Li, G. Zhang and Z. Su, *Angew. Chem., Int. Ed.*, 2016, **55**, 9239–9242.
23 K. P. Singh, E. J. Bae and J. S. Yu, *J. Am. Chem. Soc.*, 2015, **137**, 3165–3168.
24 Z. Pu, I. S. Amiinu, C. Zhang, M. Wang, Z. Kou and S. Mu, *Nanoscale*, 2017, **9**, 3555–3560.
25 W. Zhou, J. Zhou, Y. Zhou, J. Lu, K. Zhou, L. Yang, Z. Tang, L. Li and S. Chen, *Chem. Mater.*, 2015, **27**, 2026–2032.
26 Y. Yang, Z. Lun, G. Xia, F. Zheng, M. He and Q. Chen, *Energy Environ. Sci.*, 2015, **8**, 3563–3571.
27 J. Deng, P. Ren, D. Deng, L. Yu, F. Yang and X. Bao, *Energy Environ. Sci.*, 2014, **7**, 1919–1923.
28 X. Zou, X. Huang, A. Goswami, R. Silva, B. R. Sathe, E. Mikmeková and T. Asefa, *Angew. Chem., Int. Ed.*, 2014, **126**, 4461–4465.
29 Y. Zheng, Y. Jiao, L. H. Li, T. Xing, Y. Chen, M. Jaroniec and S. Qiao, *ACS Nano*, 2014, **8**, 5290–5296.
30 Y. Li, Y. Zhao, H. Cheng, Y. Hu, G. Shi, L. Dai and L. Qu, *J. Am. Chem. Soc.*, 2012, **134**, 15–18.
31 S. Yang, X. L. Feng, X. C. Wang and K. Müllen, *Angew. Chem., Int. Ed.*, 2011, **50**, 5339–5343.
32 J. Mahmood, F. Li, S. Jung, M. S. Okyay, I. Ahmad, S. J. Kim, N. Park, H. Y. Jeong and J. B. Baek, *Nat. Nanotechnol.*, 2017, **12**, 441–446.
33 Z. Wang, X. Hao, Z. Jiang, X. Sun, D. Xu, J. Wang, H. Zhong, F. Meng and X. Zhang, *J. Am. Chem. Soc.*, 2015, **137**, 15070–15703.

34 H. Duan, D. Li, Y. Tang, Y. He, S. Ji, R. Wang, H. Lv, P. P. Lopes, A. P. Paulikas, H. Li, S. X. Mao, C. Wang, N. M. Markovic, J. Li, V. R. Stamenkovic and Y. Li, *J. Am. Chem. Soc.*, 2017, **139**, 5494–5502.

35 Z. Seh, J. Kibsgaard, C. F. Dickens, I. Chorkendorff, J. K. Nørskov and T. F. Jaramillo, *Science*, 2017, **355**, 6321.

36 J. Bai, G. Xu, S. Xing, J. Zeng, J. Jiang and Y. Chen, *ACS Appl. Mater. Interfaces*, 2016, **8**, 33635–33641.

37 Z. Xing, Q. Liu, A. M. Asiri and X. Sun, *Adv. Mater.*, 2014, **26**, 5702–5707.

38 A. A. Tolia, R. J. Smiley, W. N. Delgass, C. G. Takoudis and M. J. Weaver, *J. Catal.*, 1994, **150**, 56–70.

39 K. Zhou, W. Zhou, L. Yang, J. Lu, S. Cheng, W. Mai, Z. Tang, L. Li and S. Chen, *Adv. Funct. Mater.*, 2015, **25**, 7530–7538.

40 Z. Pu, Y. Xue, I. S. Amiinu, Z. Tu, X. Liu, W. Li and S. Mu, *J. Mater. Chem. A*, 2016, **4**, 15327–15332.

41 J. Deng, P. Ren, D. Deng and X. Bao, *Angew. Chem., Int. Ed.*, 2015, **54**, 2100–2104.

42 Y. Liu, G. Yu, G. Li, Y. Sun, T. Asefa, W. Chen and X. Zou, *Angew. Chem., Int. Ed.*, 2015, **54**, 10752–10757.

43 W. Zhou, T. Xiong, C. Shi, J. Zhou, K. Zhou, N. Zhu, L. Li, Z. Tang and S. Chen, *Angew. Chem., Int. Ed.*, 2016, **128**, 8556–8560.

44 P. He, X. Yu and X. Lou, *Angew. Chem., Int. Ed.*, 2017, **56**, 3897–3900.